

# Mixed-order topology of Benalcazar-Bernevig-Hughes models

Shouvik Sur<sup>1,2,\*</sup>, Alexander C. Tyner<sup>3,\*</sup> and Pallab Goswami<sup>1,3</sup>

<sup>1</sup> *Department of Physics and Astronomy, Northwestern University, Evanston, IL 60208*

<sup>2</sup> *Department of Physics and Astronomy, Rice University, Houston, Texas 77005, USA and*

<sup>3</sup> *Graduate Program in Applied Physics, Northwestern University, Evanston, IL 60208*

(Dated: January 19, 2022)

Benalcazar-Bernevig-Hughes (BBH) models, defined on  $D$ -dimensional simple cubic lattice, are paradigmatic toy models for studying  $D$ -th order topology and corner-localized, mid-gap states. Under periodic boundary conditions, the Wilson loops of non-Abelian Berry connection of BBH models along all high-symmetry axes have been argued to exhibit gapped spectra, which predict gapped surface-states under open boundary conditions. In this work, we demonstrate the existence of cubic-symmetry-protected, gapless spectra of Wilson loops and surface-states along the body diagonal directions of the Brillouin zone. We show the gapless surface-states are described by  $2^{D-1}$ -component, massless Dirac fermions. Thus, BBH models can exhibit the signatures of first and  $D$ -th order topological insulators, depending on the details of externally imposed boundary conditions.

## I. INTRODUCTION

In quest for quantized, higher-order, electric multipole moments in crystalline systems, Benalcazar *et al.* introduced the intriguing concept of higher-order topological insulators (HOTI) [1, 2]. The gapped surface-states of these insulators were identified as lower-dimensional topological insulators (TI), giving rise to mid-gap states, localized at sharp corners and hinges of a material. The corner-localized states were argued to support topological quantization of multipole moments under suitable boundary conditions. This fascinating proposal has led to tremendous inter-disciplinary research on HOTIs [3–19], which can be realized in solid state materials [20–22], cold-atomic systems [23], photonic crystals [24–29], and mechanical meta-materials [30–40].

In spite of exciting ongoing research, the bulk topological invariants of HOTIs are still not clearly understood [1, 41–50]. Benalcazar *et al.* proposed the following topological properties of Wilson loops (WL) of non-Abelian Berry connections of HOTIs. (i) As functions of transverse momentum components, the gauge-invariant eigenvalues of WLs along high-symmetry axes (or Wannier centers) do not exhibit any non-trivial winding. (ii) The generators of WLs or Wilson loop Hamiltonians (WLH) display gapped spectra, since the mirror symmetry operators along different principal axes do not commute. (iii) The gauge-dependent WLHs of  $D$ -dimensional HOTIs are examples of  $(D - 1)$ -dimensional TIs, which can be classified within the paradigm of “nested Wilson loops” (NWL), by computing Wilson loops of Wilson loops. The NWL is a tool for dimensional reduction and topological classification of gauge-fixing ambiguities of non-Abelian Berry connections on a periodic manifold, like Brillouin zone (BZ) torus.

Since it cannot be easily implemented for complex *ab initio* band-structures of real materials, the solid-state candidates of HOTI are identified by employing

(i) complimentary analysis of various symmetry indicators and spectra of WLs under periodic boundary conditions (PBC) [44, 45, 51], and (ii) direct calculations of surface- and corner- states under open boundary conditions (OBC) [3]. The spectra of WLs for elemental bismuth have been shown to possess strongly direction-sensitive behavior. Thus, elemental bismuth has been identified as a *mixed-order topological insulator*, which can exhibit gapless or gapped surface-states, depending on the orientation of surface [16, 20, 52]. The direction-sensitive gapless surface-states also occur for anti-ferromagnetic topological insulators [53–57] and many topological crystalline insulators [58–60]. However, in real materials, due to the complexity of band structures, the precise relationship between surface-states and corner-states cannot be clearly addressed.

This has motivated us to ask the following questions for analytically controlled BBH models of  $D$ -th order TIs. (i) Can the WLs of BBH models support gapless spectra? (ii) Do BBH models support gapless surface-states along any directions? In this work, we perform explicit analytical and numerical calculations to affirmatively answer these questions and establish mixed-order topology of BBH models. We show the WLs along body-diagonal directions of cubic Brillouin zone possess gapless spectra and the gapless surface-states along body diagonals correspond to  $2^{D-1}$ -component massless, Dirac fermions. For two-dimensional BBH model of quadrupolar TIs, we also show the corner-states arise, when the flow of Dirac fermions is obstructed by boundary conditions.

## II. MODELS AND PHASE DIAGRAMS

Minimal models of first-order TIs are constructed by combining one extended  $s$ -wave function  $f_s(\mathbf{k}) = [\Delta - \sum_{j=1}^D \cos(k_j)]$  and all independent  $p$ -wave harmonics  $f_p^j(\mathbf{k}) = \sin(k_j)$  as elements of a  $(D + 1)$ -dimensional vector field

$$\mathbf{N}(\mathbf{k}) = [t_p f_p^1(\mathbf{k}), \dots, t_p f_p^D(\mathbf{k}), t_s f_s(\mathbf{k})], \quad (1)$$

\* These authors contributed equally.

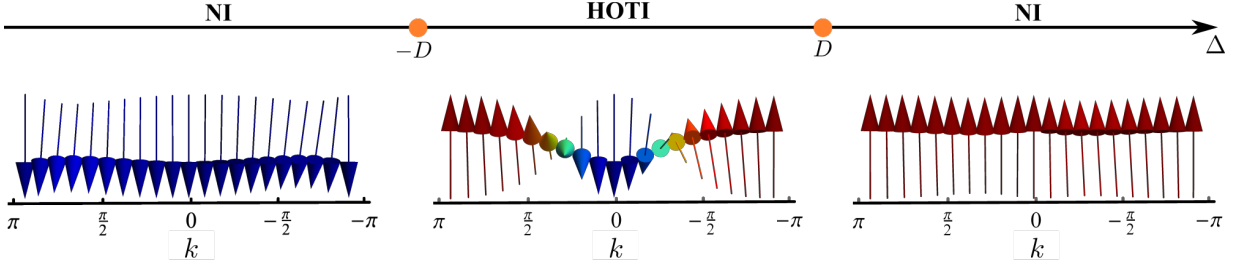


FIG. 1. The phase diagram of  $D$ -dimensional,  $D$ -th order topological insulator, described by BBH model of Eq. 4. Topologically distinct phases are separated by quantum critical points at  $|\Delta| = D$  (marked by colored dots), where bulk band gap vanishes at either the zone center or corner, thereby realizing a single, bulk Dirac point. The topologically trivial (NI) phase is distinguished from the higher-order topological insulator (HOTI) by the integer winding number of the unit vector  $\hat{\mathbf{n}}$  from Eq. 9 along the body diagonal direction of cubic Brillouin zone (shown by the texture of the arrows). Thus the difference between the NI and the HOTI can be concisely understood in terms of the first homotopy classification of Bloch Hamiltonian, along the high-symmetry lines, as proposed in the present work.

where  $t_s$  and  $t_p$  are two independent hopping parameters. The Bloch Hamiltonian  $\hat{H}_1(\mathbf{k}) = \sum_{j=1}^{D+1} N_j(\mathbf{k})\Gamma_j$  operates on  $2^s$ -component spinor  $\Psi(\mathbf{k})$ , with  $s = \lfloor \frac{D+1}{2} \rfloor$ , and  $\Gamma_j$ 's are mutually anti-commuting,  $2^s \times 2^s$  matrices. The dimensionless parameter  $\Delta$  describes band-inversion at all time-reversal-invariant momentum (TRIM) points with respect to the matrix  $\Gamma_{D+1}$ , where the  $p$ -wave harmonics vanish. Since the projection operators of conduction (+) and valence (-) bands  $P_{\pm}(\mathbf{k}) = \frac{1}{2}(\mathbb{1} \pm \hat{N}(\mathbf{k}) \cdot \mathbf{\Gamma})$  are governed by the  $O(D+1)$  unit vector  $\hat{N}(\mathbf{k}) = \mathbf{N}(\mathbf{k})/|\mathbf{N}(\mathbf{k})|$ , the bulk topological properties of  $D$ -dimensional, first order TIs are classified by the  $D$ -th spherical homotopy group  $\pi_D(S^D) = \mathbb{Z}$ .

For constructing minimal models of *cubic symmetry preserving*  $D$ -th order TIs, we have to employ  $2^D$ -component spinor  $\Psi(\mathbf{k})$  and  $2^D \times 2^D$ -dimensional, anti-commuting gamma matrices. This allows us to incorporate a *specific class of d-wave harmonics*

$$f_d^l(\mathbf{k}) = \sqrt{\frac{2}{l(l+1)}} \left[ l \cos(k_{l+1}) - \sum_{s=1}^l \cos(k_s) \right], \quad (2)$$

in the Bloch Hamiltonian, with  $l = 1, 2, \dots, (D-1)$ , and  $D \geq 2$ . Note that The role of such  $d$ -wave terms is to reduce the number of TRIM points, supporting band inversion.

The Bloch Hamiltonian of  $D$ -th order TIs can be written as  $\hat{H}_D(\mathbf{k}) = \sum_{j=1}^{2D} N_j(\mathbf{k})\Gamma_j$ , where the  $O(2D)$  vector field

$$\mathbf{N}(\mathbf{k}) = [t_p f_p^1(\mathbf{k}), \dots, t_p f_p^D(\mathbf{k}), t_d f_d^1(\mathbf{k}), \dots, t_d f_d^{D-1}(\mathbf{k}), t_s f_s(\mathbf{k})], \quad (3)$$

and  $t_s$ ,  $t_p$ , and  $t_d$  are three independent hopping param-

eters. Hence, the explicit form of  $\hat{H}_D(\mathbf{k})$  is given by

$$\hat{H}_D = t_p \sum_{j=1}^D f_p^j(\mathbf{k})\Gamma_j + t_d \sum_{j=1}^{D-1} f_d^j(\mathbf{k})\Gamma_{D+j} + t_s f_s(\mathbf{k})\Gamma_{2D}. \quad (4)$$

The form of  $\hat{H}_D$  provides a clear idea about the irreducible representations of various fermion bilinears. The mirror symmetries are implemented by

$$k_j \rightarrow -k_j, \Psi \rightarrow \hat{M}_j \Psi, \text{ with } \hat{M}_j = \frac{1}{2i}[\Gamma_j, \Gamma_{2D+1}] \quad (5)$$

with  $j = 1, 2, \dots, D$ . At  $D = 2$ , the d-wave term  $(\cos k_x - \cos k_y)$  and  $\Psi^\dagger \Gamma_3 \Psi$  transform as  $B_1$  quadrupole of  $C_{4v}$  point group. At  $D = 3$ ,  $\{\cos k_x - \cos k_y, (2 \cos k_z - \cos k_x - \cos k_y)/\sqrt{3}\}$  and  $\{\Psi^\dagger \Gamma_4 \Psi, \Psi^\dagger \Gamma_5 \Psi\}$  transform as the  $E$ -doublet of cubic point group  $O$ .

Since the absent gamma matrix  $\Gamma_{2D+1}$  anti-commutes with  $\hat{H}_D(\mathbf{k})$ , the  $D$ -th order HOTI exhibits  $\mathbb{Z}_2$  particle-hole symmetry. The operator  $\mathcal{O}(\mathbf{k}) = \Psi^\dagger(\mathbf{k})\Gamma_{2D+1}\Psi(\mathbf{k})$  has the irreducible representation of  $2^D$ -th multipole moment of  $D$ -dimensional cubic point group, which behaves as  $\prod_{i=1}^D x_i$ . For  $D = 2, 3$ , these correspond to  $B_2$  quadrupole and  $A_2$  octupole, respectively. Furthermore, all momentum dependent terms of  $\hat{H}_D$  display nesting symmetry as  $\mathbf{k} \rightarrow \mathbf{k} + (\pi, \pi, \dots, \pi)$ . The specific forms of BBH models [1, 2] can be obtained from  $\hat{H}_D(\mathbf{k})$  with special choices of hopping parameters and  $\Delta$ , viz. for  $D = 2$  [ $D = 3$ ] the parameters  $(t_s, t_p, t_d, \Delta) = (-\lambda/\sqrt{2}, \lambda, \lambda/\sqrt{2}, -2\gamma/\lambda)$  [ $(-\lambda/\sqrt{3}, \lambda, \lambda/\sqrt{2}, 0)$ ]. By setting  $t_d = 0$ , we recover models of first-order TIs, with a continuous  $O(D)$  symmetry.

The spectra of  $2^{D-1}$ -fold degenerate conduction and valence bands are given by  $E_{\pm}(\mathbf{k}) = \pm|\mathbf{N}(\mathbf{k})|$  and the phase diagram is illustrated in Fig. 1. In the parameter regime  $|\Delta| < D$ , the bands of  $D$ -th order HOTI are inverted between the center  $\mathbf{k} = (0, 0, \dots, 0)$  and the corner  $\mathbf{k} = (\pi, \pi, \dots, \pi)$  of the cubic BZ with respect to the ma-

trix  $\Gamma_{2D}$ , giving rise to a topologically non-trivial phase. The presence of band inversion at two TRIM points is due to the presence of  $d$ -wave harmonic  $f_d^{D-1}(\mathbf{k})$ . The trivial phases (NI) occurring for  $|\Delta| > D$  are separated from the non-trivial phase by topological quantum phase transitions at  $\Delta = \pm D$ . At these critical values of  $\Delta$ , the spectral gap respectively vanishes at  $\mathbf{k} = (0, 0, \dots, 0)$  and  $\mathbf{k} = (\pi, \pi, \dots, \pi)$ , while all other TRIM points remain gapped in the entire phase diagram. Therefore, the universality class of topological phase transition between a  $D$ -th order TI and NI is described by one species of  $2^D$ -component, massless Dirac fermion. By contrast, lower order TIs can support additional topologically non-trivial states, separated by band-gap closing at other TRIM points.

### III. BULK TOPOLOGICAL INVARIANTS

While the physical properties of  $\hat{H}_D$  are independent of representations of  $\Gamma$  matrices, we will assume  $\Gamma_{2D}$  to be a diagonal matrix, and other anti-commuting matrices will be chosen to have block off-diagonal forms. The projection operators of conduction and valence bands are determined by  $O(2D)$  unit vector  $\hat{N}(\mathbf{k})$ , which lies on a unit sphere  $S^n$ , with  $n = 2D - 1$ . Since,  $\pi_D(S^n)$  is trivial for any  $n > D$ , the topology of HOTIs cannot be straightforwardly described in terms of spherical homotopy classification of  $\hat{N}(\mathbf{k})$ . However, progress can be made by treating  $\hat{H}_D(\mathbf{k})$  as a non-uniform order parameter ( $\mathbf{k}$  dependent texture) that describes a pattern of symmetry breaking  $SO(2D) \rightarrow SO(2D - 1)$ . Thus,  $\hat{H}_D(\mathbf{k})$  defines map from the space group of a  $D$ -cube to the coset space  $\frac{SO(2D)}{SO(2D-1)} = \frac{Spin(2D)}{Spin(2D-1)} = S^{2D-1}$ . On fermionic spinor  $\Psi$ , the action of special orthogonal group  $SO(m)$  is realized in terms of its universal double cover group  $Spin(m)$ , such that  $SO(m) = Spin(m)/\mathbb{Z}_2$ . Consequently,  $\hat{H}_D(\mathbf{k})$  is diagonalized by unitary transformation

$$U^\dagger(\mathbf{k})\hat{H}_D(\mathbf{k})U(\mathbf{k}) = |\mathbf{N}(\mathbf{k})|\Gamma_{2D}. \quad (6)$$

Since the conduction and valence bands are  $2^{D-1}$ -fold degenerate, the diagonalizing matrix  $U(\mathbf{k})$  can only be determined up to  $Spin(2D - 1)$  gauge transformation and  $U(\mathbf{k}) \in \frac{Spin(2D)}{Spin(2D-1)}$ . Consequently, the gauge group of intra-band Berry's connection corresponds to  $SO(2D - 1) = \frac{Spin(2D-1)}{\mathbb{Z}_2}$ . A convenient form of intra-band connection is given by

$$A_\mu(\mathbf{k}) = \frac{(N_a \partial_\mu N_b - N_b \partial_\mu N_a)}{4(|\mathbf{N}| + N_{2D})} \Gamma_{ab}, \quad (7)$$

where  $\Gamma_{ab} = \frac{1}{2i}[\Gamma_a, \Gamma_b]$ , with  $a = 1, \dots, 2D - 1$ , and  $b = 1, \dots, 2D - 1$  are the generators of  $SO(2D - 1)$  group. By acting with the projection operators  $P_\pm = \frac{1}{2}(1 \pm \Gamma_{2D})$ , one arrives at Berry connections for conduction (+) and valence (-) bands.

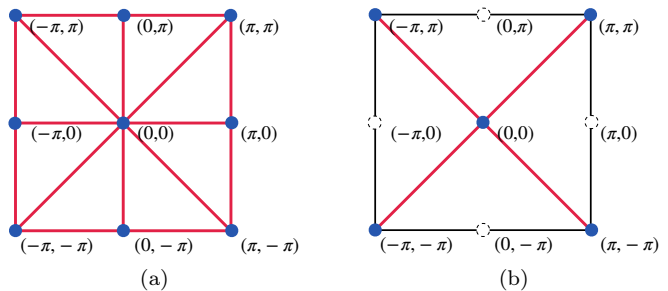


FIG. 2. Distinction between two-dimensional, first- and second-order topological insulators, based on the number of high-symmetry lines in the Brillouin zone (BZ) that can be classified by the fundamental group of a circle,  $\pi_1(S^1)$  [red lines]. (a) For first-order topological insulators (TIs), the Bloch Hamiltonian maps each line connecting two high-symmetry points (blue dots) in the BZ to a circle in the Hilbert space. Thus, all such mirror lines may be topologically classified by  $\pi_1(S^1)$ . (b) In contrast to this, for a second-order TI, exemplified by the Benalcazar-Bernevig-Hughes model, only the diagonal mirror lines can be classified by  $\pi_1(S^1)$ .

Due to the underlying cubic symmetry (symmetry of base manifold), various components of  $\mathbf{N}(\mathbf{k})$  will vanish at high-symmetry points, and on high-symmetry axes and planes, indicating partial restoration of global symmetries. Therefore, high-symmetry points, lines and planes serve as topological defects of the  $SO(2D)$ -vector field and  $SO(2D - 1)$  intra-band Berry connection. Since at the band-inversion points,  $\mathbf{N}$  has only one non-vanishing component, they support maximal restoration of the  $SO(2D - 1)$  global symmetry. Hence, these TRIM points will be mapped on to the north- and south-poles of  $S^{2D-1}$ , causing Dirac-string singularities of the Berry connection described by Eq. 7. In contrast to this, on high-symmetry axes and planes smaller sub-groups of  $SO(2D)$  are restored. The corresponding defects may be classified by one and two dimensional winding numbers. Among all high-symmetry lines (planes), the body diagonal axes (dihedral planes) connecting the points of band inversion show the maximal restoration of global symmetry and play essential roles toward topological classification.

#### A. One-dimensional winding number

Irrespective of the spatial dimensionality, all mirror-symmetry preserving  $d$ -wave harmonics ( $f_d^j$ ) vanish along the body diagonal-axes. The Bloch Hamiltonian along these lines is described by two-component vectors, indicating restoration of  $SO(2D - 2)$  global symmetry. For example, by setting  $k_x = k_y = \dots = k_D = k$ , we arrive at the following two-component model

$$\hat{H}_D(k) = t_p \sqrt{D} \sin(k)\Gamma' + [\Delta - D \cos(k)]\Gamma_{2D} \quad (8)$$

along the  $[1, 1, \dots, 1]$  direction, with  $\Gamma' = (\sum_{j=1}^D \Gamma_j)/\sqrt{D}$ . Owing to this, the two-component unit vector

$$\hat{\mathbf{n}}(k) = \frac{(t_p \sqrt{D} \sin k, \Delta - D \cos k)}{\sqrt{Dt_p^2 \sin^2 k + (\Delta - D \cos k)^2}} \quad (9)$$

describes map from a non-contractible cycle ( $S^1$ ) of the Brillouin zone to a coset space  $S^1$ , with a non-trivial winding number. When  $|\Delta| < D$ ,  $\hat{H}_D(k)$  describes a one-dimensional TI, classified by the fundamental group of a circle  $\pi_1(S^1) = \mathbb{Z}$ , which is captured by the winding of the angle

$$\theta(k) = \tan^{-1} \frac{t_p \sqrt{D} \sin k}{\Delta - D \cos k}, \quad (10)$$

as shown in Fig. 1. Since we are working with toy models with only nearest neighbor hopping, the winding number can only take values  $0, \pm 1$ . By introducing further neighbor hopping terms one can find higher winding numbers [61]. In contrast to HOTIs, first-order TIs support band inversion at all TRIM points, *and* all high-symmetry lines can be classified by  $\pi_1(S^1)$ . This distinction between first and  $D$ -th order TIs at  $D = 2$  is summarized in Fig. 2.

## B. Two-dimensional winding number

The two-dimensional (three-dimensional) HOTI also supports a rotational symmetry protected, quantized non-Abelian Berry flux through its entire bulk (dihedral planes). Because the two-dimensional HOTI is a special case of the planes in  $C_4$  rotational-symmetry protected Dirac semimetals that lie in-between the Dirac points, it can be classified by a pair of two-dimensional winding numbers [63]. The quantized flux will be associated with a specific component of the generator of  $C_4$  symmetry, which is given by the commutator of mirror operators  $\hat{M}_x$  and  $\hat{M}_y$ , i.e.,  $[\hat{M}_x, \hat{M}_y] = \Gamma_{12}$ . Here, we do not discuss it further; instead, we focus on the dihedral planes of three-dimensional HOTI.

If we consider the high-symmetry plane, which is perpendicular to  $[1, -1, 0]$  axis (exemplified by the  $k_x = k_y$  plane in Fig. 3), the Bloch Hamiltonian of 3rd-order TII will be reduced to two-dimensional,  $C_2$ -symmetric HOTI, written with  $8 \times 8$  anti-commuting matrices. If we denote  $k_{\pm} = (k_x \pm k_y)/\sqrt{2}$ , the Hamiltonian for  $[1, -1, 0]$  planes will become

$$\begin{aligned} \hat{H}_3(k_+, k_- = 0, k_z) &= \sqrt{2}t_p \sin\left(\frac{k_+}{\sqrt{2}}\right)\Gamma_+ + t_p \sin(k_z)\Gamma_3 \\ &+ \frac{2t_d}{\sqrt{3}} \left[ \cos(k_z) - \cos\left(\frac{k_+}{\sqrt{2}}\right) \right] \Gamma_5 + t_s \left[ \Delta - \cos(k_z) \right. \\ &\left. - 2 \cos\left(\frac{k_+}{\sqrt{2}}\right) \right] \Gamma_6, \end{aligned} \quad (11)$$

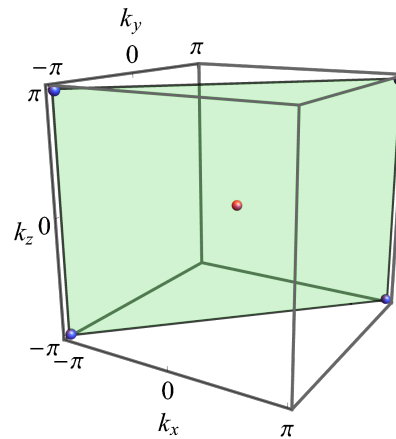


FIG. 3. One of the six dihedral planes (shaded) of three-dimensional cubic Brillouin zone, which is orthogonal to the  $[1, -1, 0]$  axis. It is a mirror plane and the red and blue dots represent the high-symmetry points that support band-inversion. The Bloch Hamiltonian for this plane has the form of two-dimensional,  $C_2$ -symmetric, Benalcazar-Bernevig-Hughes model [see Eq. 11]. The dihedral planes support  $C_2$ -symmetry protected, quantized non-Abelian Berry flux of magnitude  $2\pi$ .

and  $\Gamma_+ = (\Gamma_1 \pm \Gamma_2)/\sqrt{2}$ . The form of Hamiltonian for  $[1, 1, 0]$  plane is obtained by letting  $k_+ \rightarrow k_-$  and  $\Gamma_+ \rightarrow \Gamma_-$ . The Hamiltonian  $\hat{H}_3(k_+, k_- = 0, k_z)$  anti-commutes with  $\Gamma_4, \Gamma_-$ , and  $\Gamma_7$ . This leads to an emergent global  $SO(3)$  symmetry generated by  $\Gamma_{47}, \Gamma_{7-}$  and  $\Gamma_{4-}$ . All six dihedral planes support such emergent  $SO(3)$  symmetry with suitably defined generators. Following Ref. 63, we can show the existence of quantized, non-Abelian Berry flux of magnitude  $2\pi$  for  $[1, \pm 1, 0]$  planes, carried by generators of two-fold rotations  $\Gamma_{3\mp} = \frac{1}{2i}[\Gamma_{\mp}, \Gamma_3]$ . The presence of such non-Abelian Berry flux allows us to identify two-dimensional BBH models and the dihedral planes of three-dimensional BBH models as generalized, quantum spin Hall insulators [63]. In the following sections, we will identify the gapless spectra of WLs along the body-diagonal directions and their physical consequence.

## IV. QUADRUPOLEAR MODEL AT $D=2$

The Wilson loop  $W_{\parallel}(\mathbf{k}_{\perp})$  along the  $\hat{k}_{\parallel}$  direction is defined as

$$W_{\parallel}(\mathbf{k}_{\perp}) = \frac{1}{\mathcal{N}} \mathcal{P} \exp \left[ i \int_{-\pi}^{\pi} A_{\parallel}(k_{\parallel}, \mathbf{k}_{\perp}) dk_{\parallel} \right] \quad (12)$$

where  $\mathcal{P}$  denotes path-ordering and the  $(D - 1)$ -dimensional wave vector  $\mathbf{k}_{\perp}$  is orthogonal to  $\hat{k}_{\parallel}$ , and  $\mathcal{N}$  is the rank of gauge group. By construction  $W_{\parallel}$  is an element of the gauge group for Berry connections, transforming covariantly under  $\mathbf{k}_{\perp}$ -dependent gauge transformations. Since  $\hat{\mathbf{n}}(k)$  winds an integer number of times around  $S^1$ , the WLs along body-diagonal directions

will be mapped to non-trivial  $Z_2$  center elements  $\pm 1$  of  $Spin(2D-1)$  group. The odd (even and zero) integer winding leads to  $-1$  element ( $1$  element), which corresponds to  $\pi \bmod 2m\pi$  ( $0 \bmod 2m\pi$ ) Berry phase. The non-trivial  $\pi$  Berry phase along any high-symmetry axis is known to cause band-touching of WL bands at the projection of the axis on the transverse  $(D-1)$ -dimensional BZ. Therefore, for  $D$ -th order TIs, whether the WLH is gapless or gapped crucially depends on the direction of WL.

In order to understand the analytical structure of WLs for two-dimensional, quadrupolar insulators  $D=2$ , let us consider the components of  $Spin(3) \equiv SU(2)$  Berry connections along  $[1, \pm 1]$  directions. Without any loss of generality we can choose our  $4 \times 4$  gamma matrices to be  $\Gamma_4 = \tau_3 \otimes \sigma_0$ ,  $\Gamma_5 = \tau_2 \otimes \sigma_0$ ,  $\Gamma_j = \tau_1 \otimes \sigma_j$ , with  $j = 1, 2, 3$ . After using rotated variables  $k_{\pm} \equiv (k_x \pm k_y)/\sqrt{2}$  and the rotated components of Berry connections  $A_{\pm} = (A_x \pm A_y)/\sqrt{2}$  acquire the following form

$$A_{\pm}(\mathbf{k}) = \frac{\sqrt{2}t_p}{2N(\mathbf{k})[N(\mathbf{k}) + N_4(\mathbf{k})]} \Omega_{\pm}(k_{\mp}), \quad (13)$$

where  $N(\mathbf{k}) \equiv |N(\mathbf{k})|$ , with  $N(\mathbf{k})$  being defined by Eq. (3), and the gauge dependent matrix  $\Omega_{-s}(k_s)$  is given by

$$\Omega_{-s}(k_s) = s \sin \frac{k_s}{\sqrt{2}} \left[ t_d \sin \frac{k_s}{\sqrt{2}} (\Gamma_{23} - s\Gamma_{31}) - t_p \cos \frac{k_s}{\sqrt{2}} \Gamma_{12} \right]. \quad (14)$$

with  $s = \pm 1$ , and  $\Gamma_{12} = \tau_0 \otimes \sigma_3$ ,  $\Gamma_{23} = \tau_0 \otimes \sigma_1$ ,  $\Gamma_{31} = \tau_0 \otimes \sigma_2$  are three generators of  $SU(2)$  group. With our gauge choice, the conduction and valence bands support identical form of  $SU(2)$  Berry connection. Since  $\Omega_{+}(k_{-})$  is independent of the variable of integration  $k_{+}$ ,  $W_{+}(k_{-})$  can be calculated by performing ordinary one-dimensional integration, without bothering about discrete path-ordering procedure. Therefore, the WLHs for  $[1, \pm 1]$  directions are proportional to  $\Omega_{\pm}(k_{\mp})$  and the eigenstates of  $W_{\pm}(k_{\mp})$  correspond to those of  $\Omega_{\pm}(k_{\mp})$ . The eigenvalues of  $W_{+}(k_{-})$  are given by  $e^{\pm i\lambda_{+}(k_{-})}$ , with  $\lambda_{+}(k_{-})$  being determined by

$$\lambda_{+}(k_{-}) = \tilde{\lambda}_{+}(k_{-}) \int_{-\sqrt{2}\pi}^{\sqrt{2}\pi} dk_{+} \frac{\sqrt{2}t_p}{2N(\mathbf{k})[N(\mathbf{k}) + N_4(\mathbf{k})]}, \quad (15)$$

where  $\pm \tilde{\lambda}_{+}(k_{-})$  are eigenvalues of  $\Omega_{+}(k_{-})$ , with  $\tilde{\lambda}_{+}(k_{-}) = \sqrt{2t_d^2 \sin^4 \left( \frac{k_{-}}{\sqrt{2}} \right) + \frac{t_p^2}{4} \sin^2(\sqrt{2}k_{-})}$ .

For first-order TIs with  $t_d = 0$ ,  $\Omega_{+}(k_{-})$  vanishes at both  $k_{-} = 0$  and  $\pi/\sqrt{2}$ . At these singular locations,  $W_{+}(k_{-})$  maps to  $-1$  and  $1$ , respectively. Consequently, the WL spectra become gapless (gapped) at  $k_{-} = 0$  ( $\pi/\sqrt{2}$ ), and  $\lambda_{+}(k_{-})$  interpolates from  $0$  to  $2\pi$ . In contrast to this,  $\Omega_{+}(k_{-})$  of quadrupolar TIs vanishes only

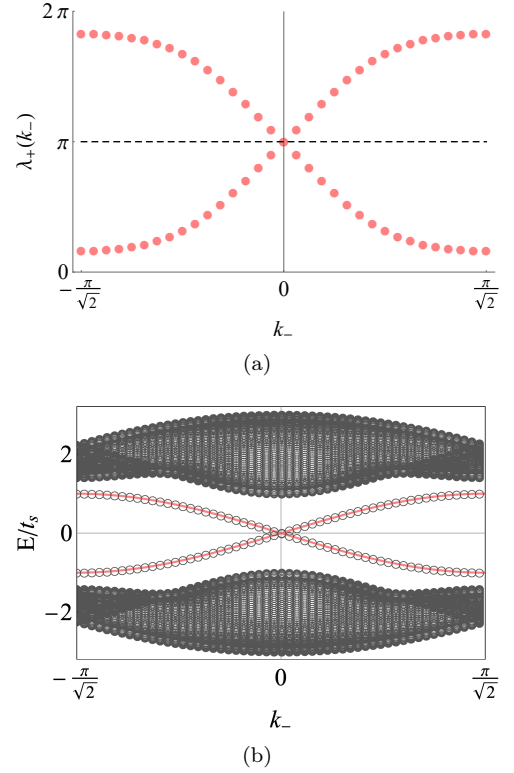


FIG. 4. Gapless spectra of Wilson loops and helical edge-states of two-dimensional, second order topological insulator along  $[1, 1]$  direction. (a) The gauge invariant spectra of Wilson loop Hamiltonian [Eq. 15] support band touching at the center of transverse/surface Brillouin zone. (b) The spectra of edge-states in the slab geometry with surfaces along the  $[1, 1]$  direction. The (gray) circles represent energy levels obtained by exact diagonalization, while the (red) solid curves are the analytically obtained dispersion [see Eq. (16)].

at  $k_{-} = 0$ . The  $d$ -wave term gives rise to non-degenerate eigenvalues of  $\Omega_{+}(k_{-})$  at  $k_{-} = \pi/\sqrt{2}$ , and  $W_{+}$  never reaches the trivial center element  $1$ . The gapless behavior of WLH is elucidated in Fig. 4a. The isolated singularity of WLH is simultaneously protected by  $C_{4v}$  and particle-hole  $Z_2$  symmetries.

The manner in which gapless WLH gives rise to gapless edge modes can also be established analytically. When the system occupies the half-space  $r_{+} > 0$ , where  $r_{+}$  is the position space conjugate of  $k_{+}$ , the analytical expressions for helical edge modes along  $[1, \pm 1]$  directions can be obtained by following Creutz and Horváth [62]. The dispersion for  $[1, 1]$  edge is given by

$$\mathcal{E}_{[11]}^{\pm}(k_{-}) = \pm \frac{\Delta t_s t_p \sin \frac{k_{-}}{\sqrt{2}}}{\sqrt{t_p^2 \sin^2 \frac{k_{-}}{\sqrt{2}} + 2t_s^2 \cos^2 \frac{k_{-}}{\sqrt{2}}}} \times \Theta \left( t_p^2 \sin^2 \frac{k_{-}}{\sqrt{2}} + 2t_s^2 \cos^2 \frac{k_{-}}{\sqrt{2}} - t_s^2 \left| \Delta \cos \frac{k_{-}}{\sqrt{2}} \right| \right), \quad (16)$$

where the Heaviside theta function,  $\Theta(x)$ , implements the condition for normalizability of the surface-states.

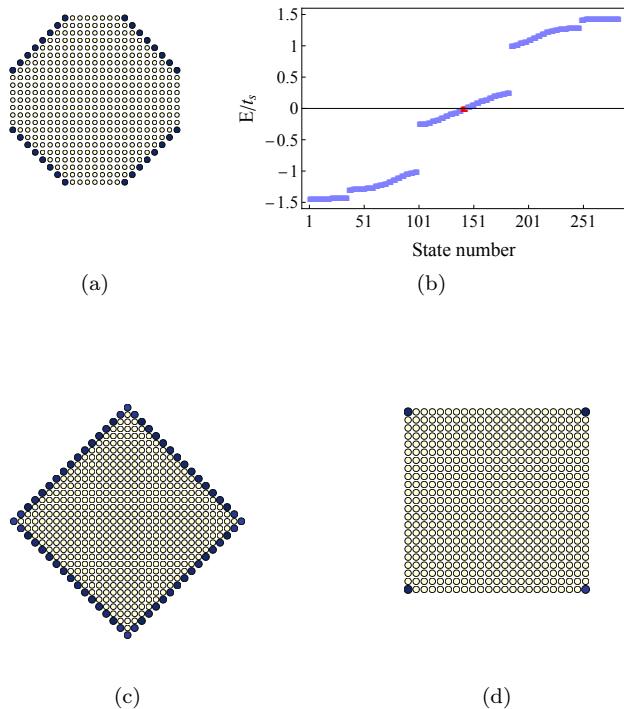


FIG. 5. Localization pattern of zero-energy states under various geometries. Here, we consider the fourfold symmetric, two-dimensional, 2nd order topological insulator described by Eq. (3). (a) A flat surface-termination is present perpendicular to all high symmetry axes in the octagonal geometry. Since only the diagonal axes support a non-trivial  $\pi_1(S^1)$  winding number, the mid-gap states are solely localized on the diagonal edges of the octagon. (b) Energy distribution of the lowest 284 states obtained by exact diagonalization in the octagonal geometry. The localization-pattern of the zero energy states (red) is given in (a). (c) If the diagonal-edges are replaced by corners, such as in the square geometry, corner-localized states are observed. (d) By contrast, if the  $x$  and  $y$  edges of the octagon are reduced to points, such as in the diamond geometry, edge propagating modes are obtained.

For  $|k_-| \ll 1$  the dispersion is linear, and describes two counter propagating modes. In Fig. 4b, we corroborate the analytically obtained edge-states dispersion by an exact diagonalization of Hamiltonian on a finite cylinder.

A similar calculation for edge-states along  $[1, 0]$  direction leads to gapped dispersion

$$\mathcal{E}_{[10]}^\pm(k_y) = \pm \sqrt{(t_p \sin k_y)^2 + \frac{(t_s t_d)^2}{t_s^2 + t_d^2} (\Delta - 2 \cos k_y)^2} \times \Theta((t_d^2 + t_s^2) - |(t_d^2 - t_s^2) \cos k_y + t_s^2 \Delta|), \quad (17)$$

in agreement with Refs. 1 and 2. For the special choice of parameters in the BBH model [1],  $|t_s| = |t_d|$ , the  $\Theta(x)$ -function is independent of  $k_y$ , and the surface bands are normalizable at all  $k_y \in (-\pi, \pi]$ . However, for general model parameters, the gapped edge-modes are normaliz-

able over a restricted region of surface BZ.

Therefore, our detailed analysis of two-dimensional HOTI clearly reveals the following mixed-order topological properties: the bulk is a generalized quantum spin Hall state that supports (i) quantized, non-Abelian Berry flux of magnitude  $2\pi$ ; (ii) the presence of gapless (gapped) WLHs along  $[1, \pm 1]$  ( $[1, 0]$  and  $[0, 1]$ ) directions; and (iii) the existence of gapless helical (gapped) edge-modes along  $[1, \pm 1]$  ( $[1, 0]$  and  $[0, 1]$ ) directions. Next we demonstrate that the corner-states emerge, when the flow of helical edge-states is hindered by boundary conditions.

In finite samples, the localization pattern of the topologically protected mid-gap states is strongly geometry dependent. For any  $D$ -dimensional point group, there exists a sample-geometry with  $(D - 1)$ -dimensional surface terminations perpendicular to every high-symmetry axes. The localization pattern of the mid-gap states in such a geometry bears a direct correspondence with the  $\pi_1(S^1)$ -based classification of the bulk topology. In particular, if a high-symmetry axis supports a non-trivial  $\pi_1(S^1)$  winding number under periodic boundary condition, then the surface-terminations perpendicular to it will support  $(D - 1)$ -dimensional edge-localized states. In Fig. 5(a), we demonstrate this principle through the localization pattern of the mid-gap states in the two-dimensional 2nd-order TI in an octagonal geometry. Because the diagonal-axes carry non-trivial  $\pi_1(S^1)$  windings, the zero-energy states [see Fig. 5(b)] are localized only on the diagonal edges of the octagon. If the  $x$  and  $y$  [diagonal] edges are reduced to points, then the zero-energy states are localized along the edges [at the corners] of the resultant diamond- [square-] shaped samples, as shown in Fig. 5(c)[(d)]. Therefore, in the diamond geometry, the two-dimensional 2nd-order TI supports propagating edge-localized states. It is, thus, notable that the mid-gap states in an HOTI may behave like those in 1st-order TIs under suitable sample geometries. In the following section, we identify the analytical structure of WLH and gapless surface-states at  $D = 3$ .

## V. OCTUPOLAR MODEL AT $D=3$

The  $\pi_1(S^1)$  classification of  $[1, 1, 1]$  axis [see Eq. 9] and  $C_2$ -symmetric BBH form at  $[1, -1, 0]$  dihedral plane [see Eq. 11] indicate the presence of gapless WL bands and surface-states. Without any loss of generality, we will use the following representation of  $8 \times 8$  gamma matrices:  $\Gamma_6 = \eta_3 \mathbb{1}_{4 \times 4}$ ,  $\Gamma_7 = \eta_2 \otimes \mathbb{1}_{4 \times 4}$ , and  $\Gamma_j = \eta_1 \otimes \gamma_j$ , where  $\gamma_j$ 's are five mutually anticommuting  $4 \times 4$  matrices. For calculating WL of  $SO(5)$  Berry connection along  $[1, 1, 1]$  direction, it is convenient to use the rotated coordinates

$$(k_1, k_2, k_3) \equiv \left( \frac{k_x - k_y}{\sqrt{2}}, \frac{k_x + k_y - 2k_z}{\sqrt{6}}, \frac{k_x + k_y + k_z}{\sqrt{3}} \right) \quad (18)$$

and the rotated component  $A_3 = (A_x + A_y + A_z)/\sqrt{3}$  of Berry connection, whose form is given by

$$A_3(\mathbf{k}) = \frac{1}{2N(\mathbf{k})[N(\mathbf{k}) + N_6(\mathbf{k})]} \Omega_3(k_1, k_2). \quad (19)$$

The WLH will be proportional to the gauge dependent matrix

$$\begin{aligned} \Omega_3(k_1, k_2) = & \frac{1}{\sqrt{3}} \left[ t_p^2 \sin(\sqrt{2}k_1) \Gamma_{12} + t_p^2 \sin\left(\frac{k_1}{\sqrt{2}} + \frac{\sqrt{3}k_2}{\sqrt{2}}\right) \Gamma_{13} - t_p^2 \sin\left(\frac{k_1}{\sqrt{2}} - \frac{\sqrt{3}k_2}{\sqrt{2}}\right) \Gamma_{23} \right. \\ & + 2t_p t_d \sin^2 \frac{k_1}{\sqrt{2}} (\Gamma_{14} - \Gamma_{24}) - 2t_p t_d \sin \frac{k_1}{\sqrt{2}} \sin \frac{\sqrt{3}k_2}{\sqrt{2}} \Gamma_{34} + \frac{t_p t_d}{\sqrt{3}} \left\{ 1 + \cos(\sqrt{2}k_1) - 2 \cos\left(\frac{k_1}{\sqrt{2}} + \frac{\sqrt{3}k_2}{\sqrt{2}}\right) \right\} \Gamma_{15} \\ & + \frac{t_p t_d}{\sqrt{3}} \left\{ 1 + \cos(\sqrt{2}k_1) - 2 \cos\left(\frac{k_1}{\sqrt{2}} - \frac{\sqrt{3}k_2}{\sqrt{2}}\right) \right\} \Gamma_{25} - \frac{2t_p t_d}{\sqrt{3}} \left\{ 1 - \cos \frac{k_1}{\sqrt{2}} \cos \frac{\sqrt{3}k_2}{\sqrt{2}} \right\} \Gamma_{35} \\ & \left. + \frac{4t_d^2}{\sqrt{3}} \sin \frac{k_1}{\sqrt{2}} \left( \cos \frac{k_1}{\sqrt{2}} - \cos \frac{\sqrt{3}k_2}{\sqrt{2}} \right) \Gamma_{45} \right], \end{aligned} \quad (20)$$

which is independent of  $k_3$ . Since  $\Omega_3$  is independent of  $k_3$ , the WL is easily obtained by performing one-dimensional integration over  $k_3$ , and the WLH is proportional to  $\Omega_3$ . The  $8 \times 8$  matrices  $\Gamma_{ab} = [\Gamma_a, \Gamma_b]/(2i)$  correspond to ten generators of  $SO(5)$  group, and they can also be expressed as  $\Gamma_{ab} = \eta_0 \otimes \gamma_{ab}$ , where  $\gamma_{ab}$  are  $4 \times 4$  generators of  $SO(5)$  group. Therefore, identical form of Berry connection for conduction and valence bands will be found by acting with projectors  $P_{\pm} = \frac{1}{2}(1 \pm \Gamma_6)$ . The projections of  $\Omega_3(k_1, k_2)$  on conduction and valence bands can be obtained from Eq. 20, with the replacement  $\Gamma_{ab} \rightarrow \gamma_{ab}$ . Although all  $SO(5)$  generators simultaneously appear in  $\Omega_3(k_1, k_2)$ , it can be shown that  $\Omega_3^2(k_1, k_2) \propto 1$ . Consequently, at any generic location of  $(k_1, k_2)$ -plane, the eigenvalues of WLH will be two-fold degenerate. Since the eigenstates of  $\Omega_3(k_1, k_2)$  are also the eigenstates of  $W_3(k_1, k_2)$ ,  $\Omega_3(k_1, k_2)$  describes  $SO(5)/SO(4)$  gauge fixing of Berry connection.

For first-order TIs,  $\Omega_3(k_1, k_2)$  vanishes at  $\bar{\Gamma}$  :  $(k_1, k_2) = (0, 0)$ , and  $\bar{M}$  :  $(k_1, k_2) = (0, 0)$  points of the hexagonal, transverse or surface BZ. Furthermore,  $W_3$  maps to  $-\mathbb{1}$  and  $\mathbb{1}$  at  $\bar{\Gamma}$  and  $\bar{M}$  points, respectively. This gives rise to the interpolation of WLH spectra ( $\pm\lambda_3$ ) between 0 and  $2\pi$ . In contrast to this,  $\Omega_3(k_1, k_2)$  for octupolar TIs only vanishes at  $\bar{\Gamma}$ . As  $d$ -wave terms gap out WLH spectra at  $\bar{M}$  point, the WL of octupolar TI cannot interpolate between  $\pm\mathbb{1}$ . The behavior of  $\lambda_3(k_1, k_2)$  is shown in Fig. 6a. Due to the four-fold degeneracy of WLH spectra at  $\bar{\Gamma}$  point, we expect the surface-states for (111) surface to be described by four-component, massless Dirac fermions. For the BBH model *augmented by a finite  $\Delta$* , the surface-states close to the zone center obtain an isotropic dispersion,

$$\mathcal{E}_{(111)}^{\pm}(k_1, k_2) \approx \pm \frac{t_p \Delta}{3} \sqrt{k_1^2 + k_2^2}. \quad (21)$$

With increasing deviations from the zone center, the Dirac cone acquires a trigonal warping due to the three-fold rotational symmetry about the  $[1\ 1\ 1]$  axis [see Appendix A for more details]. We note that for the BBH model of a three-dimensional 3rd order TI  $\Delta = 0$ , which would lead to flat surface states. The solution of surface-states dispersion is illustrated in Fig.6b and the detailed form is presented in Appendix A. We further note that the spin-orbital texture of surface-states in the immediate vicinity of Dirac point can be reasonably approximated by linearized form of  $\Omega_3$ , which allows us to identify the surface Dirac point as  $SO(5)$  vortex.

In contrast to the surfaces perpendicular to the body-diagonals, surface terminations along the principal axes host gapped surface-states [1, 2]. We exemplify the dispersion of these gapped states on the (001) surface,

$$\begin{aligned} \mathcal{E}_{(001)}^{\pm}(k_x, k_y) = & \pm \Theta(1 - f_2^2) [t_p^2 (\sin^2 k_x + \sin^2 k_y) \\ & + t_d^2 (\cos k_x - \cos k_y)^2 + \alpha^2 t_s^2 (\Delta - f_1)^2]^{1/2}, \end{aligned} \quad (22)$$

where  $\alpha^{-1} = \sqrt{4t_d^2 + 3t_s^2}/(2|t_d|)$ ,  $f_1 = 3(\cos k_x + \cos k_y)/2$ , and  $f_2 = [3t_s^2 \Delta + (2t_d^2 - 3t_s^2)f_1]/(3t_s^2 + 4t_d^2)$ . For generic hopping parameters, the doubly degenerate conduction and valence bands do not extend over the entire surface Brillouin zone.

## VI. DISCUSSION

In this work we formulated a unified, gauge-invariant description of bulk-topology through first-homotopy classification of high-symmetry lines and second homotopy classification of high-symmetry planes. Our analytical results show that the Wilson loop spectra of HOTIs have strong direction dependence. The presence of band-

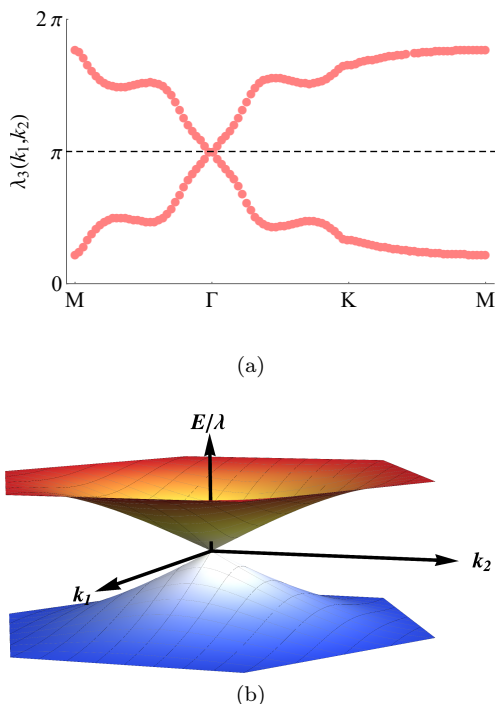


FIG. 6. Gapless behavior of Wilson loop Hamiltonian and surface-states of three-dimensional, octupolar topological insulator along  $[1, 1, 1]$  direction. (a) The Wilson loop bands are two-fold degenerate and exhibit four-fold degeneracy only at the center of hexagonal, surface Brillouin zone. (b) The two-fold degenerate surface- conduction and valence bands meet at the Dirac point located at the center of surface Brillouin zone. Here,  $k_1$  and  $k_2$  axes are perpendicular to the  $[111]$  direction, and we have set  $(t_s, t_p, t_d) = (-\frac{\lambda}{\sqrt{3}}, \lambda, \frac{\lambda}{\sqrt{2}})$  with  $\lambda$  and  $\Delta > 0$ .

inversion between the center and the corner of cubic Brillouin zone gives rise to gapless (gapped) spectra along body diagonals (principal axes). Consequently,  $D$ -th order TIs support gapless (gapped) surface-states along the body diagonal (principal axes). In the class of models we considered here, the gapless surface-states take the form of  $(D - 1)$ -dimensional Dirac fermions. For similar reasons, gapless surface states are also present in  $n$ -th order TIs with  $n \leq D$  under suitable sample geometries. *Since recent experiments on engineered systems have simulated quadrupolar and octupolar topological insulators, our predictions for the gapless surface states and their relationship with corner-states can be directly verified with such experimental set up.*

Since topologically protected states at crystal terminations play a key role in determining the nature of bulk-topology, corner or hinge localized states have been designated as the defining signatures of higher order topology. Due to their sub-extensive nature, however, such states are usually not accessible to angle resolved photoemission spectroscopy, which is a powerful probe for elucidating band-topology of solid-state systems. The Dirac-like surface-state we obtain here, therefore, offers

an avenue for angle resolved photoemission spectroscopy, to directly address higher order topology, if a suitable cleavage surface is available. Further, our results indicate the need for distinguishing between surface state signatures of higher-order and weak topology, as both may support Dirac cones on a subset of crystalline-symmetry preserving surface terminations.

Our analysis can also be applied to other models of HOTIs, with stronger resemblance to 1st-order TIs. An interesting class of such models is obtained by using  $^D C_2$  number of  $\sin k_a \sin k_b$  type  $d$ -wave harmonics, which are odd under the mirror operation  $k_a \rightarrow -k_a$  (or  $k_b \rightarrow -k_b$ ). At  $D = 2$ , this corresponds to replacing  $B_1$  harmonic ( $\cos k_x - \cos k_y$ ) in Eq. 3 by  $B_2$  harmonic  $\sin k_x \sin k_y$  of  $C_{4v}$  point group. Akin to the 1st-order TI, the resulting model supports band inversion at all TRIM points, and admits Fu-Kane's  $\mathbb{Z}_2$  index. The Wilson lines along principal axes display gapless spectra and  $\lambda_x(k_y)$  interpolates between 0 and  $2\pi$  (winding of Wannier charge centers). Consequently, under the slab geometry along principal axes and the square geometry of Fig. 5d one finds gapless helical edge-modes, which connect bulk conduction and valence bands. *However, the Wilson lines and the surface-states along  $[1, \pm 1]$  directions display gapped spectra.* Therefore, under open boundary conditions with diamond geometry of Fig. 5c, one obtains gapped edge modes and zero-energy, corner-localized, mid-gap states. The induced quadrupole moment will have  $B_1$  symmetry. Here, we learn an important lesson: *all high-symmetry lines joining band-inversion points are not required to support  $\pi$  Berry phase or time-reversal polarization, and there exist HOTI models that display fully connected spectra of Wilson lines along principal axes.*

Finally we note that two-dimensional, topological insulators with gapped Wilson loop and edge spectra along all high-symmetry directions can be obtained by combining both  $B_1$  and  $B_2$  harmonics on an equal footing. The resulting  $C_4$ -symmetric models lack  $\mathbb{Z}_2$  particle-hole symmetry of BBH type models and describe generic planes of Dirac semimetals, which are orthogonal to the direction of nodal separation. Due to the lack of  $\mathbb{Z}_2$  particle-hole symmetry, the four-fold degenerate corner-states can be found under the square and the diamond geometries. Such models can be called "ideal HOTI" due to the absence of gapless edge-state, or "beyond 2nd order" TI as the corner-states occur at non-zero energy. The quantized non-Abelian Berry flux constitutes the robust bulk invariant for such ideal HOTIs [63].

## ACKNOWLEDGMENTS

This work was supported by the National Science Foundation MRSEC program (DMR-1720139) at the Materials Research Center of Northwestern University. The work of S.S. at Rice University was supported by the U.S. Department of Energy Computational Materials Sciences (CMS) program under Award Number DE-

SC0020177. S.S. would like to thank Ming Yi for helpful

discussions. The plots in Fig. 5 were produced by the *Pybinding* package [64].

- 
- [1] W.A. Benalcazar, B.A. Bernevig, and T.L. Hughes, *Science* **357**, 61 (2017).
- [2] W.A. Benalcazar, B.A. Bernevig, and T.L. Hughes, *Phys. Rev. B* **96**, 245115 (2017).
- [3] Josias Langbehn, Yang Peng, Luka Trifunovic, Felix von Oppen, and Piet W. Brouwer, *Phys. Rev. Lett.* **119**, 246401 (2017).
- [4] W. A. Benalcazar, T. Li, and T. L. Hughes, *Phys. Rev. B* **99**, 245151 (2019).
- [5] Zhida Song, Zhong Fang, and Chen Fang, *Phys. Rev. Lett.* **119**, 246402 (2017).
- [6] Guido van Miert and Carmine Ortix, *Phys. Rev. B* **98**, 081110(R) (2018).
- [7] Yuxuan Wang, Mao Lin, and Taylor L. Hughes, *Phys. Rev. B* **98**, 165144 (2018).
- [8] Flore K. Kunst, Guido van Miert, and Emil J. Bergholtz, *Phys. Rev. B* **97**, 241405(R) (2018).
- [9] V. Dwivedi, C. Hickey, T. Eschmann, and S. Trebst, *Phys. Rev. B* **98**, 054432 (2018).
- [10] M. Ezawa *Phys. Rev. Lett.* **120**, 026801 (2018).
- [11] Y. You, D. Litinski, and F. von Oppen, *Phys. Rev. B* **100**, 054513 (2019).
- [12] E. Lee, R. Kim, J. Ahn, and B.-J. Yang, *npj Quantum Materials* **5**, 1 (2020).
- [13] M. Rodriguez-Vega, A. Kumar, and B. Seradjeh, *Phys. Rev. B* **100**, 085138 (2019).
- [14] D. Varjas, A. Lau, K. Pöyhönen, A. R. Akhmerov, D. I. Pikulin, and I. C. Fulga, *Phys. Rev. Lett.* **123**, 196401 (2019).
- [15] R. Chen, C.-Z. Chen, J.-H. Gao, B. Zhou, and D.-H. Xu, *Phys. Rev. Lett.* **124**, 036803 (2020).
- [16] F. Schindler, A.M. Cook, M.G. Vergniory, Z. Wang, S.S.P. Parkin, B. Andrei Bernevig, and T. Neupert, *Sci. Adv.* **4**, (2018).
- [17] Dumitru Călugăru, Vladimir Juričić, and Bitan Roy, *Phys. Rev. B* **99**, 041301(R) (2019).
- [18] Weixuan Zhang, Deyuan Zou, Qingsong Pei, Wenjing He, Jiacheng Bao, Houjun Sun, and Xiangdong Zhang *Phys. Rev. Lett.* **126**, 146802 (2021)
- [19] Biye Xie, Hai-Xiao Wang, Xiujuan Zhang, Peng Zhan, Jian-Hua Jiang, Minghui Lu, and Yanfeng Chen, *Nature Reviews Physics* **3**, 520 (2021).
- [20] F. Schindler, Z. Wang, M.G. Vergniory, A.M. Cook, A. Murani, S. Sengupta, A.Y. Kasumov, R. Deblock, S. Jeon, I. Drozdov, H. Bouchiat, S. Guéron, A. Yazdani, B.A. Bernevig, and T. Neupert, *Nat. Phys.* **14**, 918 (2018).
- [21] Berthold Jäck, Yonglong Xie, Jian Li, Sangjun Jeon, B Andrei Bernevig, and Ali Yazdani, *Science* **364**, 1255 (2019).
- [22] Berthold Jäck, Yonglong Xie, B Andrei Bernevig, and Ali Yazdani, *PNAS* **117**, 16214 (2020).
- [23] S. N. Kempkes, M. R. Slot, J. J. van Den Broeke, P. Capiod, W. A. Benalcazar, D. Vanmaekelbergh, D. Bercioux, I. Swart, and C. Morais Smith, *Nat. Mat.* **18**, 1292 (2019).
- [24] Jiho Noh, Wladimir A Benalcazar, Sheng Huang, Matthew J Collins, Kevin P Chen, Taylor L Hughes, and Mikael C Rechtsman, *Nature Photonics* **12**, 408 (2018).
- [25] Ashraf El Hassan, Flore K Kunst, Alexander Moritz, Guillermo Andler, Emil J Bergholtz, and Mohamed Bourennane., *Nature Photonics* **13**, 697 (2019).
- [26] Sunil Mittal, Venkata Vikram Orre, Guanyu Zhu, Maxim A. Gorlach, Alexander Poddubny, and Mohammad Hafezi, *Nature Photonics* **13**, 692 (2019).
- [27] Xiao-Dong Chen, Wei-Min Deng, Fu-Long Shi, Fu-Li Zhao, Min Chen, and Jian-Wen Dong , *Phys. Rev. Lett.* **122**, 233902 (2019).
- [28] B.-Y. Xie, G.-X. Su, Hong-Fei Wang, Hai Su, Xiao-Peng Shen, Peng Zhan, Ming-Hui Lu, Zhen-Lin Wang, and Yan-Feng Chen *Phys. Rev. Lett.* **122**, 233903 (2019).
- [29] Yang Liu, Shuwai Leung, Fei-Fei Li, Zhi-Kang Lin, Xiufeng Tao, Yin Poo, and Jian-Hua Jiang, *Nature* **589**, 381–385 (2021)
- [30] Xiang Ni, Matthew Weiner, Andrea Alù, and Alexander B Khanikaev, *Nature Materials* **18**, 113 (2019).
- [31] S. Imhof, C. Berger, F. Bayer, J. Brehm, L. W. Molenkamp, T. Kiessling, F. Schindler, C. H. Lee, M. Greiter, T. Neupert, and R. Thomale, *Nat. Phys.* **14**, 925 (2018).
- [32] Christopher W Peterson, Wladimir A Benalcazar, Taylor L Hughes, and Gaurav Bahl., *Nature* **555**, 346 (2018).
- [33] Marc Serra-Garcia, Valerio Peri, Roman Süsstrunk, Osama R Bilal, Tom Larsen, Luis Guillermo Villanueva, and Sebastian D Huber, *Nature* **555**, pages342 (2018).
- [34] Haoran Xue, Yahui Yang, Fei Gao, Yidong Chong, and Baile Zhang, *Nature Materials* **18**, 108 (2019).
- [35] Haoran Xue, Yahui Yang, Guigeng Liu, Fei Gao, Yidong Chong, and Baile Zhang, *Phys. Rev. Lett.* **122**, 244301 (2019).
- [36] Xiujuan Zhang, Hai-Xiao Wang, Zhi-Kang Lin, Yuan Tian, Biye Xie, Ming-Hui Lu, Yan-Feng Chen, and Jian-Hua Jiang, *Nature Physics* **15**, 582 (2019).
- [37] Haiyan Fan, Baizhan Xia, Liang Tong, Shengjie Zheng, and Dejie Yu, *Phys. Rev. Lett.* **122**, 204301 (2019).
- [38] Haoran Xue, Yong Ge, Hong-Xiang Sun, Qiang Wang, Ding Jia, Yi-Jun Guan, Shou-Qi Yuan, Yidong Chong, and Baile Zhang *Nat. Commun.* **11**, 2442 (2020).
- [39] Xiang Ni, Mengyao Li, Matthew Weiner, Andrea Alù, and Alexander B. Khanikaev, *Nat. Commun.* **11**, 2108 (2020).
- [40] Christopher W. Peterson, Tianhe Li, Wladimir A. Benalcazar, Taylor L. Hughes, and Gaurav Bahl, *Science* **368**, 1114 (2020)
- [41] Max Geier, Luka Trifunovic, Max Hoskam, and Piet W. Brouwer, *Phys. Rev. B* **97**, 205135 (2018).
- [42] K. Shiozaki and M. Sato, *Phys. Rev. B* **90**, 165114 (2014).
- [43] L. Trifunovic and P.W. Brouwer, *Phys. Rev. X* **9**, 011012 (2019).
- [44] E. Khalaf, *Phys. Rev. B* **97**, 205136 (2018).
- [45] Eslam Khalaf, Hoi Chun Po, Ashvin Vishwanath, and Haruki Watanabe, *Phys. Rev. X* **8**, 031070 (2018).
- [46] F. Schindler, M. Brzezinska, W. A. Benalcazar, M. Iraola, A. Bouhon, S. S. Tsirkin, M. G. Vergniory, and T. Neu-

- pert, *Phys. Rev. Res.* **1**, 033074 (2019).
- [47] J. Ahn and B.-J. Yang, *Phys. Rev. B* **99**, 235125 (2019).
- [48] Nobuyuki Okuma, Masatoshi Sato, and Ken Shiozaki, *Phys. Rev. B* **99**, 085127 (2019).
- [49] Elis Roberts, Jan Behrends, and Benjamin Béri, *Phys. Rev. B* **101**, 155133 (2020).
- [50] Bitan Roy and Vladimir Juričić *Phys. Rev. Research* **3**, 033107 (2021).
- [51] A. Bouhon, A. M. Black-Schaffer, and R.-J. Slager, *Phys. Rev. B* **100**, 195135 (2019).
- [52] Chuang-Han Hsu, Xiaoting Zhou, Tay-Rong Chang, Qiong Ma, Nuh Gedik, Arun Bansil, Su-Yang Xu, Hsin Lin, and Liang Fu, *PNAS* **116**, 13255 (2019).
- [53] Roger S. K. Mong, Andrew M. Essin, and Joel E. Moore *Phys. Rev. B* **81**, 245209 (2010).
- [54] Mikhail M. Otrokov, Ilya I. Klimovskikh, Hendrik Bentmann, Alexander Zeugner, Ziya S. Aliev, Sebastian Gass, Anja U. B. Wolter, Alexandra V. Koroleva, Dmitry Estyunin, Alexander M. Shikin, María Blanco-Rey, Martin Hoffmann, Alexandra Yu. Vyazovskaya, Sergey V. Eremeev, Yury M. Koroteev, Imamaddin R. Amiraslanov, Mahammad B. Babanly, Nazim T. Mamedov, Nadir A. Abdullayev, Vladimir N. Zverev, Bernd Büchner, Eike F. Schwier, Shiv Kumar, Akio Kimura, Luca Petaccia, Giovanni Di Santo, Raphael C. Vidal, Sonja Schatz, Katharina Kiskner, Chul-Hee Min, Simon K. Moser, Thiago R. F. Peixoto, Friedrich Reinert, Arthur Ernst, Pedro M. Echenique, Anna Isaeva, and Evgueni V. Chulkov, *Nature* **576**, 416 (2019).
- [55] Hang Li, Shun-Ye Gao, Shao-Feng Duan, Yuan-Feng Xu, Ke-Jia Zhu, Shang-Jie Tian, Jia-Cheng Gao, Wen-Hui Fan, Zhi-Cheng Rao, Jie-Rui Huang, Jia-Jun Li, Da-Yu Yan, Zheng-Tai Liu, Wan-Ling Liu, Yao-Bo Huang, Yu-Liang Li, Yi Liu, Guo-Bin Zhang, Peng Zhang, Takeshi Kondo, Shik Shin, He-Chang Lei, You-Guo Shi, Wen-Tao Zhang, Hong-Ming Weng, Tian Qian, Hong Ding, *Phys. Rev. X* **9**, 041039 (2019).
- [56] Y. J. Chen, L. X. Xu, J. H. Li, Y. W. Li, H. Y. Wang, C. F. Zhang, H. Li, Y. Wu, A. J. Liang, C. Chen, S. W. Jung, C. Cacho, Y. H. Mao, S. Liu, M. X. Wang, Y. F. Guo, Y. Xu, Z. K. Liu, L. X. Yang, and Y. L. Chen, *Phys. Rev. X* **9**, 041040 (2019).
- [57] Yu-Jie Hao, Pengfei Liu, Yue Feng, Xiao-Ming Ma, Eike F. Schwier, Masashi Arita, Shiv Kumar, Chaowei Hu, Rui'e Lu, Meng Zeng, Yuan Wang, Zhanyang Hao, Hong-Yi Sun, Ke Zhang, Jiawei Mei, Ni Ni, Liusuo Wu, Kenya Shimada, Chaoyu Chen, Qihang Liu, and Chang Liu, *Phys. Rev. X* **9**, 041038 (2019).
- [58] Hoi Chun Po, Ashvin Vishwanath, and Haruki Watanabe, *Nat. Commun.* **8**, 50 (2017).
- [59] Barry Bradlyn, L. Elcoro, Jennifer Cano, M. G. Vergniory, Zhijun Wang, C. Felser, M. I. Aroyo, and B. Andrei Bernevig, *Nature* **547**, 298 (2017).
- [60] Ru Chen, Hoi Chun Po, Jeffrey B. Neaton, and Ashvin Vishwanath, *Nat. Phys.* **14**, 55 (2017).
- [61] Y. Wang, S. Sur, A. C. Tyner, and P. Goswami, (in preparation).
- [62] M. Creutz and I. Horvath, *Phys. Rev. D* **50**, 2297 (1994).
- [63] A. C. Tyner, S. Sur, D. Puggioni, J. M. Rondinelli, and P. Goswami, arXiv:2012.12906.
- [64] D. Moldovan, M. Andelković, and F. Peeters, pybinding v0.9.5: a Python package for tight-binding calculations (v0.9.5), Zenodo (2020).

### Appendix A: Gapless surface-states of octupolar model

Here, we note the key intermediate steps for the derivation of the [111] surface states. In the  $(k_1, k_2, k_3)$  coordinates the Hamiltonian takes the form,

$$H_{D=3} = \mathbf{N} \cdot \mathbf{\Gamma}', \quad (\text{A1})$$

where  $\mathbf{\Gamma}'$  are a set of 6 mutually anti-commuting  $8 \times 8$  matrices, and

$$\begin{aligned} \frac{N_1}{t_p} &= \cos \frac{k_3}{\sqrt{3}} \left[ \sin \frac{k_1}{\sqrt{2}} \cos \frac{k_2}{\sqrt{6}} + \sin \frac{k_2}{\sqrt{6}} \cos \frac{k_1}{\sqrt{2}} \right] + \sin \frac{k_3}{\sqrt{3}} \left[ \cos \frac{k_1}{\sqrt{2}} \cos \frac{k_2}{\sqrt{6}} - \sin \frac{k_1}{\sqrt{2}} \sin \frac{k_2}{\sqrt{6}} \right] \\ \frac{N_2}{t_p} &= \cos \frac{k_3}{\sqrt{3}} \left[ \sin \frac{k_2}{\sqrt{6}} \cos \frac{k_1}{\sqrt{2}} - \sin \frac{k_1}{\sqrt{2}} \cos \frac{k_2}{\sqrt{6}} \right] + \sin \frac{k_3}{\sqrt{3}} \left[ \sin \frac{k_1}{\sqrt{2}} \sin \frac{k_2}{\sqrt{6}} + \cos \frac{k_1}{\sqrt{2}} \cos \frac{k_2}{\sqrt{6}} \right] \\ \frac{N_3}{t_p} &= \sin \frac{k_3}{\sqrt{3}} \cos \left( \sqrt{\frac{2}{3}} k_2 \right) - \sin \left( \sqrt{\frac{2}{3}} k_2 \right) \cos \frac{k_3}{\sqrt{3}} \\ \frac{N_4}{2t_d} &= \sin \frac{k_1}{\sqrt{2}} \sin \frac{k_3}{\sqrt{3}} \cos \frac{k_2}{\sqrt{6}} + \sin \frac{k_1}{\sqrt{2}} \sin \frac{k_2}{\sqrt{6}} \cos \frac{k_3}{\sqrt{3}} \\ \frac{\sqrt{3}N_5}{2t_d} &= \cos \frac{k_3}{\sqrt{3}} \left[ \cos \left( \sqrt{\frac{2}{3}} k_2 \right) - \cos \frac{k_1}{\sqrt{2}} \cos \frac{k_2}{\sqrt{6}} \right] + \sin \frac{k_3}{\sqrt{3}} \left[ \sin \left( \sqrt{\frac{2}{3}} k_2 \right) + \sin \frac{k_2}{\sqrt{6}} \cos \frac{k_1}{\sqrt{2}} \right] \\ \frac{N_6}{t_s} &= \cos \frac{k_3}{\sqrt{3}} \left[ -2 \cos \frac{k_1}{\sqrt{2}} \cos \frac{k_2}{\sqrt{6}} - \cos \left( \sqrt{\frac{2}{3}} k_2 \right) \right] + \sin \frac{k_3}{\sqrt{3}} \left[ 2 \sin \frac{k_2}{\sqrt{6}} \cos \frac{k_1}{\sqrt{2}} - \sin \left( \sqrt{\frac{2}{3}} k_2 \right) \right] + \Delta. \end{aligned} \quad (\text{A2})$$

After a sequence of unitary transformations one can solve for the states on the (111) surface for the system occupying the half space  $r_3 > 0$  (or, equivalently,  $r_3 < 0$ ), where  $r_3$  is the position space conjugate of  $k_3$ . We find a pair of twofold degenerate bands, described by

$$\mathcal{E}_{(111)}(k_1, k_2) = \pm |t_s \Delta| \sqrt{(\cos \theta_3 \sin \theta_5 \sin \phi_1)^2 + (\cos \theta_3 \sin \theta_5 \cos \phi_1 \cos \phi_2 + \sin \theta_3 \sin \phi_2)^2}, \quad (\text{A3})$$

where

$$\begin{aligned} \theta_1 &= \tan^{-1} \frac{\sin \left( \frac{k_1}{\sqrt{2}} + \frac{k_2}{\sqrt{6}} \right)}{\sin \left( \frac{k_1}{\sqrt{2}} - \frac{k_2}{\sqrt{6}} \right)}; & \theta_2 &= -\tan^{-1} \frac{t_p \cos \frac{k_2}{\sqrt{6}}}{t_d \sin \frac{k_1}{\sqrt{2}}}; & \theta_3 &= \tan^{-1} \frac{2t_d \left[ \cos \left( \frac{2}{\sqrt{6}} k_2 \right) - \cos \frac{k_1}{\sqrt{2}} \cos \frac{k_2}{\sqrt{6}} \right]}{\sqrt{3}t_s \left[ \cos \left( \frac{2}{\sqrt{6}} k_2 \right) + 2 \cos \frac{k_1}{\sqrt{2}} \cos \frac{k_2}{\sqrt{6}} \right]}; \\ f_1 &= \sqrt{\sin^2 \left( \frac{k_1}{\sqrt{2}} + \frac{k_2}{\sqrt{6}} \right) + \sin^2 \left( \frac{k_1}{\sqrt{2}} - \frac{k_2}{\sqrt{6}} \right)}; & f_2 &= \sqrt{\left( t_p \cos \frac{k_2}{\sqrt{6}} \right)^2 + \left( t_d \sin \frac{k_1}{\sqrt{2}} \right)^2}; \\ f_3 &= \sqrt{(2t_d)^2 \left[ \cos \left( \frac{2}{\sqrt{6}} k_2 \right) - \cos \frac{k_1}{\sqrt{2}} \cos \frac{k_2}{\sqrt{6}} \right]^2 + (\sqrt{3}t_s)^2 \left[ \cos \left( \frac{2}{\sqrt{6}} k_2 \right) + 2 \cos \frac{k_1}{\sqrt{2}} \cos \frac{k_2}{\sqrt{6}} \right]^2}; \\ \theta_4 &= \tan^{-1} \frac{t_p f_1}{f_2}; & \theta_5 &= \tan^{-1} \frac{\sqrt{t_p^2 f_1^2 + f_2^2}}{f_3}; \\ \tilde{g}_1 &= \cos \theta_1 g_1 + \sin \theta_1 g_2; & \tilde{g}_2 &= -\cos \theta_4 (\sin \theta_1 g_1 - \cos \theta_1 g_2) - \sin \theta_4 (\sin \theta_2 g_3 + \cos \theta_2 g_4); \\ \tilde{g}_3 &= \cos \theta_2 g_3 - \sin \theta_2 g_4; & \tilde{g}_5 &= \cos \theta_3 g_5 + \sin \theta_3 g_6 \\ \tilde{g}_4 &= \cos \theta_5 [\sin \theta_4 (\cos \theta_1 g_2 - \sin \theta_1 g_1) + \cos \theta_4 (\sin \theta_2 g_3 + \cos \theta_2 g_4)] + \sin \theta_5 [\sin \theta_3 g_5 - \cos \theta_3 g_6] \\ \phi_1 &= \tan^{-1} \frac{\sqrt{\tilde{g}_1^2 + \tilde{g}_2^2 + \tilde{g}_3^2}}{\tilde{g}_4}; & \phi_2 &= \tan^{-1} \frac{\sqrt{\tilde{g}_1^2 + \tilde{g}_2^2 + \tilde{g}_3^2 + \tilde{g}_4^2}}{\tilde{g}_5}, \end{aligned} \quad (\text{A4})$$

with  $g_j$  being the coefficient of  $\Gamma'_j$  multiplying  $\sin \frac{k_3}{\sqrt{3}}$  in Eq. (A1).

The conduction and valence bands are two-fold degenerate and display four-fold degeneracy only at the center of

hexagonal surface BZ. Close to the zone center, in terms of  $\{k_\perp, \phi\} = \{\sqrt{k_1^2 + k_2^2}, \arctan(k_2/k_1)\}$ ,

$$\begin{aligned} \frac{\mathcal{E}_{(111)}(k_\perp, \phi)}{|t_s \Delta|} &= \frac{|t_p|}{3|t_s|} k_\perp + \frac{3(t_d^2 + 2t_p^2)t_s^2 - 4t_p^4}{216|t_p||t_s|^3} k_\perp^3 \\ &+ \frac{12t_s^2 t_p^4 (t_s^2 (8 \cos(6\phi) + 5) - 10t_d^2) - 60t_d^2 t_p^2 t_s^4 (5 \cos(6\phi) - 7) + 15t_d^4 t_s^4 (16 \cos(6\phi) - 17) - 240t_p^6 t_s^2 + 80t_p^8}{51840|t_p|^3 |t_s|^5} k_\perp^5 + o(k_\perp^7), \end{aligned} \quad (\text{A5})$$

which leads to the asymptotic form of the dispersion noted in the main section of the paper. We note that the warping term arises at  $o(k_\perp^5)$ , and it is present at  $t_d = 0$ , i.e. for 1st order TIs.